On the modelling of the switching mechanisms of a Coanda fluidic oscillator

Shiqi Wang, Ahmad Batikh, Lucien Baldas, Azeddine Kourta, Nicolas Mazellier, Stéphane Colin, Stéphane Orieux

On the modelling of the switching mechanisms of a Coanda fluidic oscillator

Shiqi Wang[a,b], Ahmad Batikh[a,*], Lucien Baldas[a], Azeddine Kourta[c], Nicolas Mazellier[c], Stéphane Colin[a], Stéphane. Orieux[a]

[a] *Institut Clément Ader (ICA), Université de Toulouse, CNRS, INSA, ISAE-SUPAERO, Mines-Albi, UPS, Toulouse, France*

[b] *Aero-Engine Academy of China, Aero-Engine Corporation of China, Beijing, 101304, China*

[c] *Université d'Orléans; INSA-CVL; PRISME EA 4229, Orléans, F45072, France*

Abstract

A Coanda fluidic oscillator has been studied numerically and experimentally to understand the internal switching mechanism and to estimate the frequency of resulting pulsed jets. 2D numerical simulations were performed and the oscillator switching mechanism was unveiled. The results of the simulation confirmed that the pressure difference between the two control ports and the pressure difference between the two branches control the oscillation dynamics of the oscillator. A detailed function defining the pulsation frequency has been proposed, taking into account the forth and back velocities of the pressure wave in the feedback loops which are difficult to measure experimentally. A simplified form of the frequency function has thus been proposed. An experimental study was performed to validate the numerical results, using two oscillator prototypes having the same central part but different feedback loop configurations. The experimental results confirmed the frequency function proposed from the computational study. The effects of the inlet pressure and the length of feedback loops have been experimentally

* Corresponding author.

E-mail address: ahmad.batikh@insa-toulouse.fr

studied. It has been found that with a given feedback loop, the oscillation period initially decreases as the input pressure increases.

Key words

Fluidic oscillator, Coanda effect, Active flow control, CFD, Hot-wire anemometry

1 Nomenclature & abbreviations

C_0	Speed of sound in ambient environment (m/s)
f	Oscillation frequency (Hz)
L_f	Feedback loop length (m)
Ma	Mach number
u	Local fluid velocity in the feedback loop (m/s)
$\overline{u}$	Average fluid velocity in the feedback loop (m/s)
t	Time (s)
T	Oscillation period (s)
$\Delta P_{\mathrm{P1-P2}}$	Pressure difference between the control ports at the jet base (Pa)
$\Delta P_{\mathrm{A1-A2}}$	Pressure difference between the two main branches (Pa)
$\Delta P_{\mathrm{B1-B2}}$	Pressure difference between the branch center sections (Pa)
ε	Error term
τ_t	Transmission time (s)
τ_s	Switching time (s)
ZNMF	Zero net mass flux
MEMS	Micro-electro-mechanical-systems
MFJ	Main flow jet
HPCW	High pressure compression wave
LPEW	Low pressure expansion wave

2 Introduction

For many decades, fluidic actuators have attracted the attention of researchers for their high potential for a wide range of applications, such as reducing drag on bluff bodies [1], increasing lift of airfoils [2,3], enhancing mixing in combustion chambers [4,5] or enhancing heat transfer [6,7]. Unsteady actuation appears as a much more attractive strategy than steady actuation to enhance the efficiency of the system, for instance by increasing the entrainment of momentum in active flow control applications (see e.g. [8,9]) or heat transfer rate of an impinging jet [10]. These periodic fluidic disturbances can be provided by various kinds of actuators [11] such as zero net mass flux (ZNMF) actuators, plasma actuators or micro-electro-mechanical-systems (MEMS). Among them, fluidic oscillators can emit oscillating jets in a large operating frequency and velocity range when supplied with a pressurized fluid. They do not require any moving part, since their oscillations are totally self-induced and self-sustained and only depend on the internal flow dynamics. All in all, these properties yield highly reliable and robust actuation system, which are mandatory from industrial scope [12–14].

According to Gregory [15], fluidic oscillators can be classified into two main categories based on their underlying oscillation mechanism. The first kind of oscillator is the wall-attachment fluidic oscillator, the principle of which is based on the Coanda effect; it is thus also called Coanda oscillator. The second kind of oscillator is the jet-interaction fluidic oscillator with a principle based on complex interaction dynamics inside a cavity. Raghu proposed in his work [16] a slightly different classification by discriminating the oscillators between switching (or pulsing) jet fluidic oscillators and sweeping jet fluidic oscillators based on the different patterns of the generated jets. On the one hand, a sweeping jet oscillator has only one outlet through which an undulant jet issues, regardless of its feedback mechanism [17] or jet-interaction mechanism [18]. On the other hand, pulsing jet fluidic oscillators (Fig. 1) usually consist of one inlet supplied at constant pressure and two outlets, between which the flow switches alternatively. Even though a number of studies have been devoted to the pulsing jet oscillator for the purpose of different applications [19–21], the physical mechanisms responsible for the jet switching are still misunderstood. Accordingly, the design of such devices remains based on trial and error procedures. One of the reasons for that is the difficulty to access the inner flow by means of experimental methods. A comprehensive understanding of the switching mechanism is however essential to design properly this kind of actuator.

The behavior of the pulsing jet fluidic oscillator is based on the Coanda effect as shown in Fig. 1: the jet issuing from nozzle N attaches one of the two walls, W1 or W2, depending for instance on the initial conditions. If there was no feedback loops and if the outlet sections were large, the attachment to wall W1 or wall W2 would be stable and the flow would exit through the corresponding outlet, O1 or O2, respectively. With feedback loops, when the jet is attached to wall W1, part of the flow fills in the feedback loop F1 due to the hydraulic restriction at outlet O1. This yields a pressure increase in the left side of the device (in this particular example), which eventually promotes the jet switching. In an equivalent manner, the same phenomenon develops in the right side of the oscillator and results in a self-sustained oscillating behavior, with a pulsed flow alternatively exiting outlets O1 and O2.

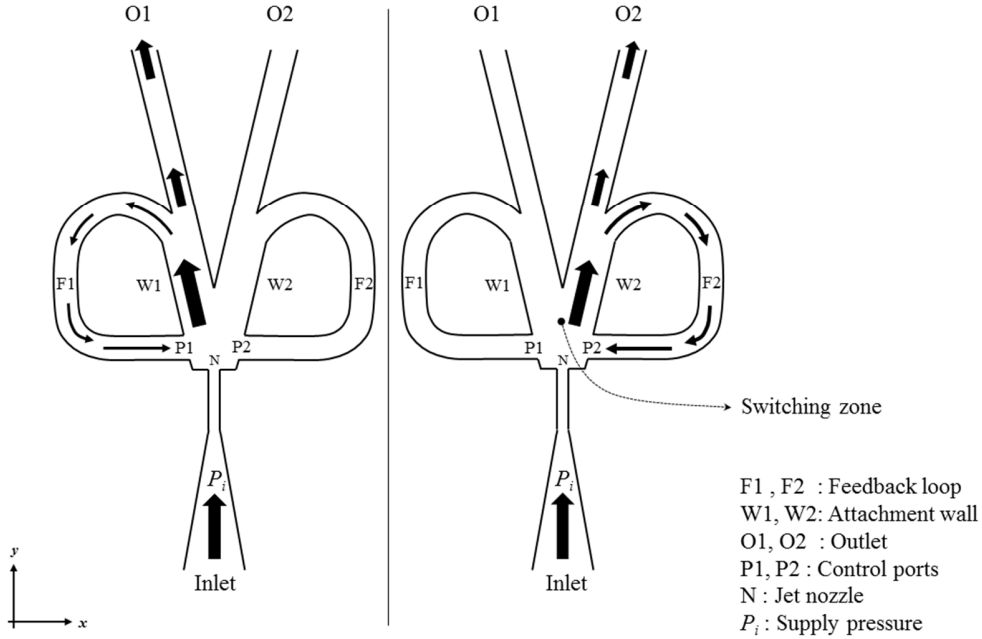

Fig. 1. Illustration of the basic configuration of a pulsing jet Coanda fluidic oscillator, adapted from [22]

One of the main features of the pulsing jet is the oscillation frequency. Several studies, such as [23–27], showed that the feedback loop length and diameter, the size and design of control ports P1 and P2, as well as the properties of the operating fluid play an important role in determining the oscillation frequency. In addition, there exists a pressure difference threshold between the control ports, above which the jet switching happens [28]. With fixed geometry and operating fluid, the frequency increases as the inlet pressure increases. This adds some

complexity for analyzing the effectiveness of certain applications, as active flow control, since the frequency correlates with the injection momentum, which is dependent on the inlet pressure.

However, in a pulsing jet fluidic oscillator, it is possible to have a quasi-constant frequency response, independent to the inlet pressure. In the studies of Cerretelli et al. [12,19], two oscillators are exploited: the first one is almost pressure-controlled and its frequency varies with the inlet pressure, while the second one is almost pressure-insensitive and operates at a constant frequency under the same inlet pressure range. Nevertheless, their different frequency response behaviors have not been clearly explained. In another study by Tesař [29] about this kind of oscillator, it is also demonstrated that the oscillation frequency is neither proportional to the inlet flow rate as in the case of a sonic fluidic oscillator [29], nor kept constant as in the study of Cerretelli and Gharaibah [12]. No complete physical explanation has been proposed yet to the different frequency response patterns of this type of oscillator. Furthermore, Simões et al. [30] experimentally and numerically investigated a fluidic oscillator with both liquid and gas as working fluids. They proposed a correlation law to express the relationship between the switching frequency and the length of the feedback loop as:

$$f = 1/[2(\tau_t + \tau_s)] = 2[(L_f / C_0) + (\xi h / U)] \quad (1)$$

where τ_t , τ_s are the transmission time of pressure wave through the feedback loop and the switching time respectively, C_0 the sound velocity, L_f the feedback loop length, h the nozzle-to-splitter distance, U the jet velocity and ξ an empirical constant. However, it is not clear how this law was established, and thereby if it can be extrapolated to different designs of Coanda fluidic oscillators (for instance when varying the distance between control ports and nozzle).

In the present study, the behavior of a Coanda fluidic oscillator is investigated over a large range of operating conditions in order to bring a better understanding of the physical mechanisms at the root of this kind of pulsing jet oscillator. The three above mentioned frequency response patterns (frequency proportional to the inlet flow rate, constant frequency, or more complex behavior) were reproduced with the same oscillator core just by modifying its feedback loops volume. A detailed computational study of the internal flow pattern was conducted and the switching mechanism was described in a fully detailed way. The frequency response of the oscillator was explored and a new switching model was proposed and validated by a complete experimental study. Following this analysis, a new and

simple function to estimate the operating frequency is proposed, as a guiding tool for the design of pulsing jets oscillators.

The paper is organized as follows. The geometry of the model oscillator used in this study, the numerical simulations settings and the experimental set-up are described in Section 3. The computational study of the internal flow pattern and the effect of the supply pressure on the oscillator behavior are reported in Sections 4 and 5, respectively, while the experimental results are presented and analyzed in Section 6. The main conclusions from this study and some perspectives for future work are given in the last section.

3 Oscillator model description

For getting a better understanding of the oscillator flow dynamics, both numerical and experimental studies were performed in this work in a very complementary approach. On the one hand, the numerical model allows a detailed analysis of the internal flow pattern, which is difficult to realize experimentally, but essential to study the internal oscillation mechanisms of the device. On the other hand the experimental approach allows to validate numerical results and to complete the study to unveil the key parameters of the Coanda fluidic oscillator. For these reasons, a fully 2-D shape oscillator is proposed with large depth over transversal lengths ratios. The use of two-dimensional geometric shapes not only reduces the cost of a numerical calculation, but also makes it easy to compare the results of the computational study with those of the experimental study. Fig. 2 shows a sketch of the proposed oscillator with key dimensions and a more detailed view of the central part (switching zone) is proposed in Fig. 3. This design is basically composed of a nozzle N, 200µm in width, two feedback loops F1 and F2 connected to two control ports P1 and P2 and two outputs O1 and O2, 500µm in width. It is worth noticing that there is no offset along the *y*-axis between control ports P1 and P2 and the nozzle inlet, unlike many other actuator designs found in the literature (e.g. [22], see Fig. 1).

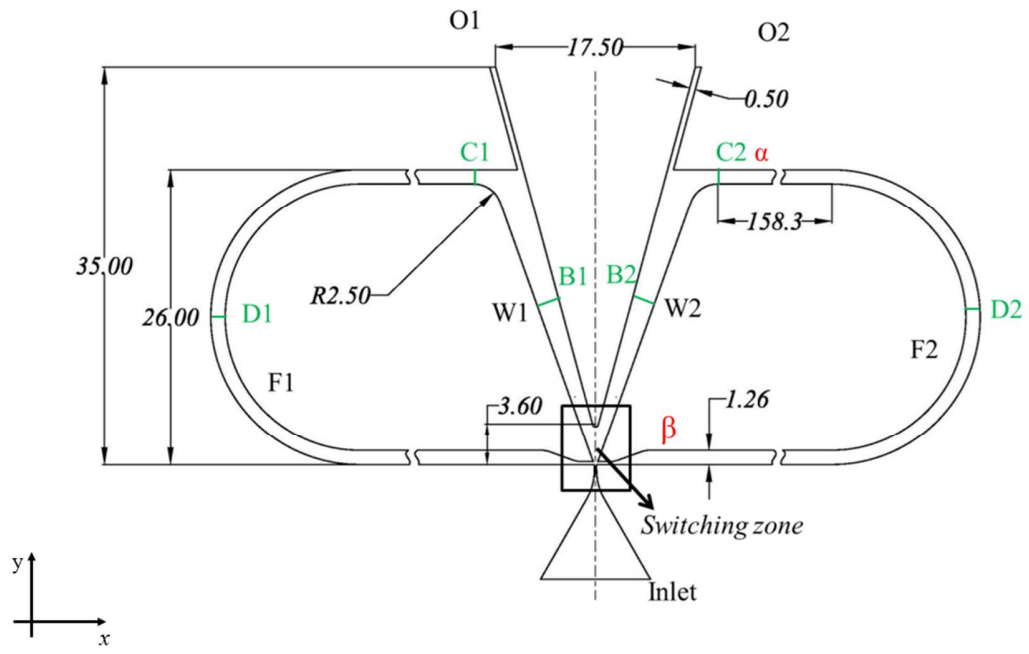

Fig. 2. Sketch and key dimensions (in mm) of the oscillator

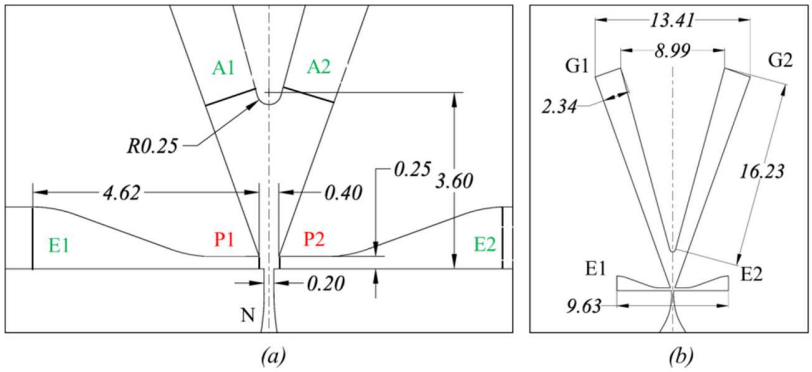

Fig. 3. (a) Details of the switching zone of the oscillator (in mm); (b) Simplified central part of a typical oscillator

3.1 Numerical settings

The 2-D simulations were performed on the geometry previously detailed in Fig. 2. A pressure condition was set for both the inlet and the outlet limits of the computational domain; with a limited inlet absolute total pressure up to 0.25 MPa, and an outlet absolute static pressure of 0.1 MPa in sections O1 and O2. The working fluid was air

considered as a perfect gas with the following properties: molar mass M = 28.9 g/mol, specific heat capacity at constant pressure c_p = 1005 J/kg K, dynamic viscosity μ = 1.8 10^{-05} Pa s, Prandtl number Pr = 0.7.

The open source CFD solver OpenFOAM has been chosen to implement the numerical simulations for its ability to deal with complex geometries and its high parallel computation capability. After a detailed study of the sensitivity of various numerical schemes, including the turbulence model, mesh density, temporal and spatial discretization schemes, Courant number choices, and considering both the numerical precision and the calculation cost, the schemes chosen in the following series of simulations are the following: sonicFoam solver, realizable k-epsilon turbulence model, 2nd order upwind schemes in spatial terms, backward 2nd order scheme in temporal term, and a maximum local Courant Number limited to 0.3 with a time step of 4×10^{-9} s. The grid density at the wall permits to obtain an average value of the dimensionless wall distance y^+ of the order of 10, compatible with the used standard wall function. The mesh consists of quadrangle cells only in order to get high mesh quality. The total cell number is 1.2×10^5, with 20 nodes in the throat part and 15 nodes in both outlet sections. In order to reach a regular periodic behavior (a statistically stable behavior), more than 20 periods were simulated.

3.2 Experimental setup

For the experimental study, two oscillators, called Osc.1 and Osc.2, have been designed, manufactured and tested (Fig. 4). Both designs have an identical central part (switching zone) which is exactly the same as the one used in the numerical work. However, Osc.1 has a complete "two-dimensional" design (including the feedback loops in the same plane) with a uniform depth of 10 mm (i.e. much larger than the width of the internal channels of the device); the measured frequencies and outlet velocities can then be compared to 2D simulation results. On the other hand, feedback loops F1 and F2 of Osc.2 can be changed by linking ports α and β (see Fig. 2) using plastic tubes with various lengths (200, 300, 400, 500, 600, and 766 mm). The extremities of these tubes are connected to ports α and β, perpendicularly to the plane. Tubes with an internal diameter of 4 mm are used in Osc.2 to have the same cross-sectional area than the feedback loops of Osc.1.

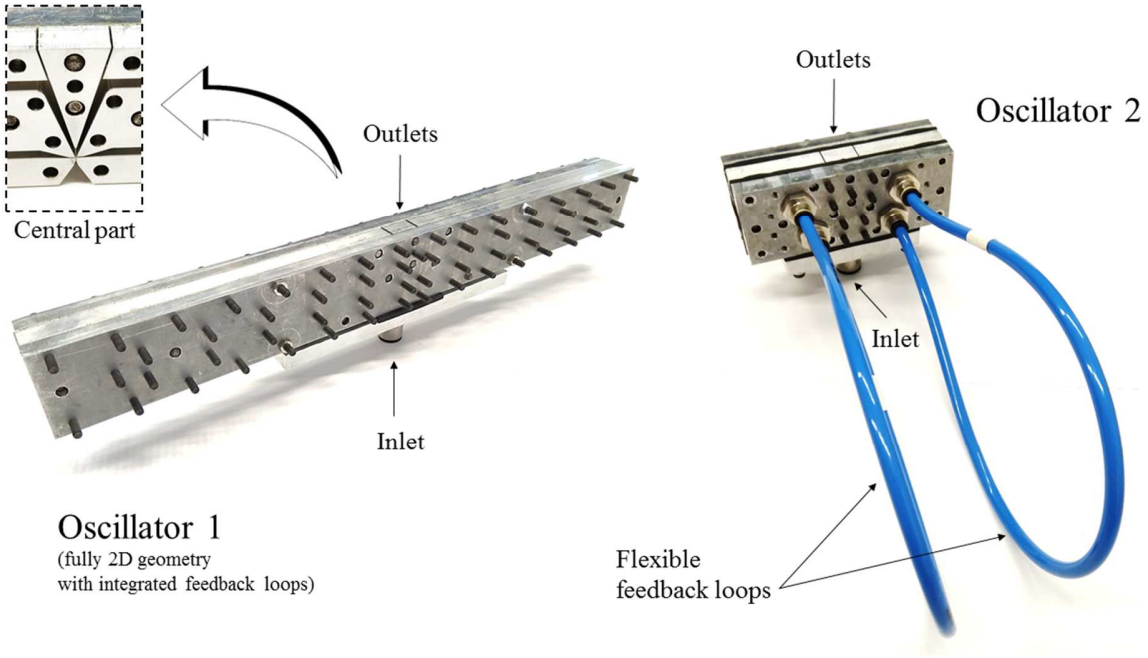

Fig. 4. Osc.1 (left) and Osc.2 (right) with the same central part used in the experimental study

In order to obtain working frequency and outlet velocity profiles of the oscillator, two measurement techniques were employed: a hot wire anemometry and a transient pressure measurement with a transducer. The hot wire anemometry can measure the outlet velocity profile while providing the oscillator working frequency. The hot wire, however, is so fragile that it was only employed in low inlet pressure conditions, while the pressure transducer can be used in a wide range of inlet pressures. Thus, the velocity in the axis of each outlet of the oscillator was measured by a TSI 1210-T1.5 hot wire for inlet total pressure ranging only from 0.1 to 0.3 MPa, while the frequency responses were provided by an Endevco 8510B-200 pressure sensor for a wider inlet pressure range, from 0.1 to 0.7 MPa. The sampling frequency was 25 kHz and the signal was recorded during 10 s.

4 Computational study of the flow patterns inside the fluidic oscillator

The main goal of this computational study was to provide a better understanding of the inner flow to get new insights about the physical mechanisms underlying the switching process. A detailed analysis of the jet switching process inside the oscillator has been performed by comparing the pressure and velocity contours at key instants and by examining the evolution with time of the area-weighted average pressure and velocity magnitude in various sections along the feedback loops and at the exit of the oscillator [31]. It has been found that the jet oscillation

frequency has a direct relationship with the forth and back propagation of the pressure wave in the feedback loop. The switching of the jet would then result from both the pressure difference between the control ports at the jet base, $\Delta P_{P1-P2} = P_{P1} - P_{P2}$, and the pressure difference between the two main branches, $\Delta P_{A1-A2} = P_{A1} - P_{A2}$ (see Fig. 3a for the location of sections A and P). In order to clarify this idea, an in-depth analysis coupling global (frequency response at the oscillator's outlets) and local (switching mechanisms at the jet nozzle) flow dynamics is required.

By considering several reference times to illustrate the oscillation process, the periodic behavior can be observed on the evolution of area-averaged velocities in *y*-direction (see Fig. 2) at both oscillator outlets presented in Fig. 5, and on the evolution of the pressure differences ΔP_{P1-P2} and ΔP_{A1-A2} as well as the pressure difference between the branch center sections, $\Delta P_{B1-B2} = P_{B1} - P_{B2}$ (see Fig. 2 for the location of sections B) presented in Fig. 6, together with snapshots of velocity contours at four characteristic times of the first half period in order to illustrate the jet switching mechanism. In addition, a video showing the evolution with time of the pressure and the velocity in the oscillator over one period has been provided as supplementary material (video.SM01) for a better visualization of the jet switching phenomenon.

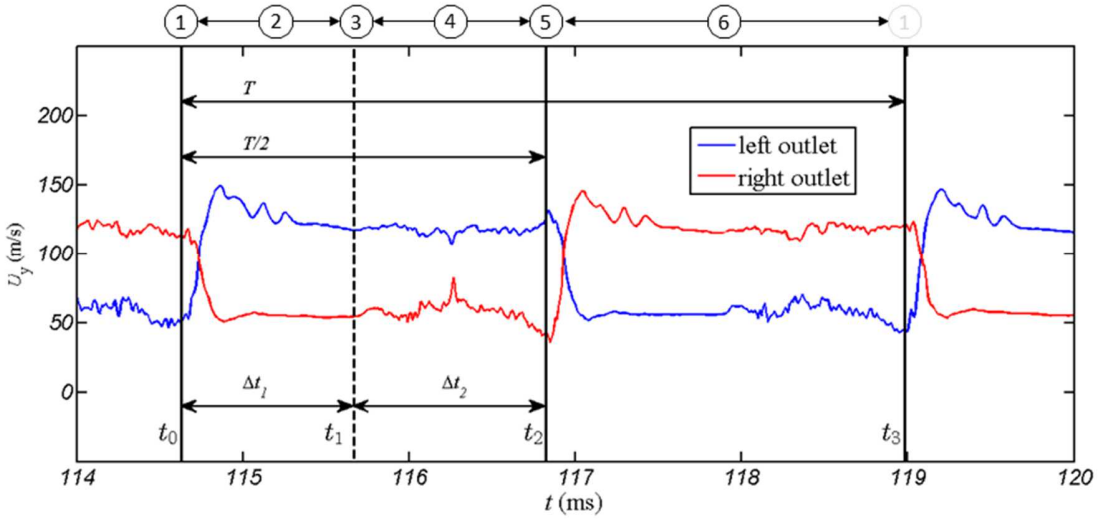

Fig. 5. Evolution of the area-averaged velocity magnitude U_y at both outlets with time - Numerical simulation for $P_i = 0.25\,MPa$

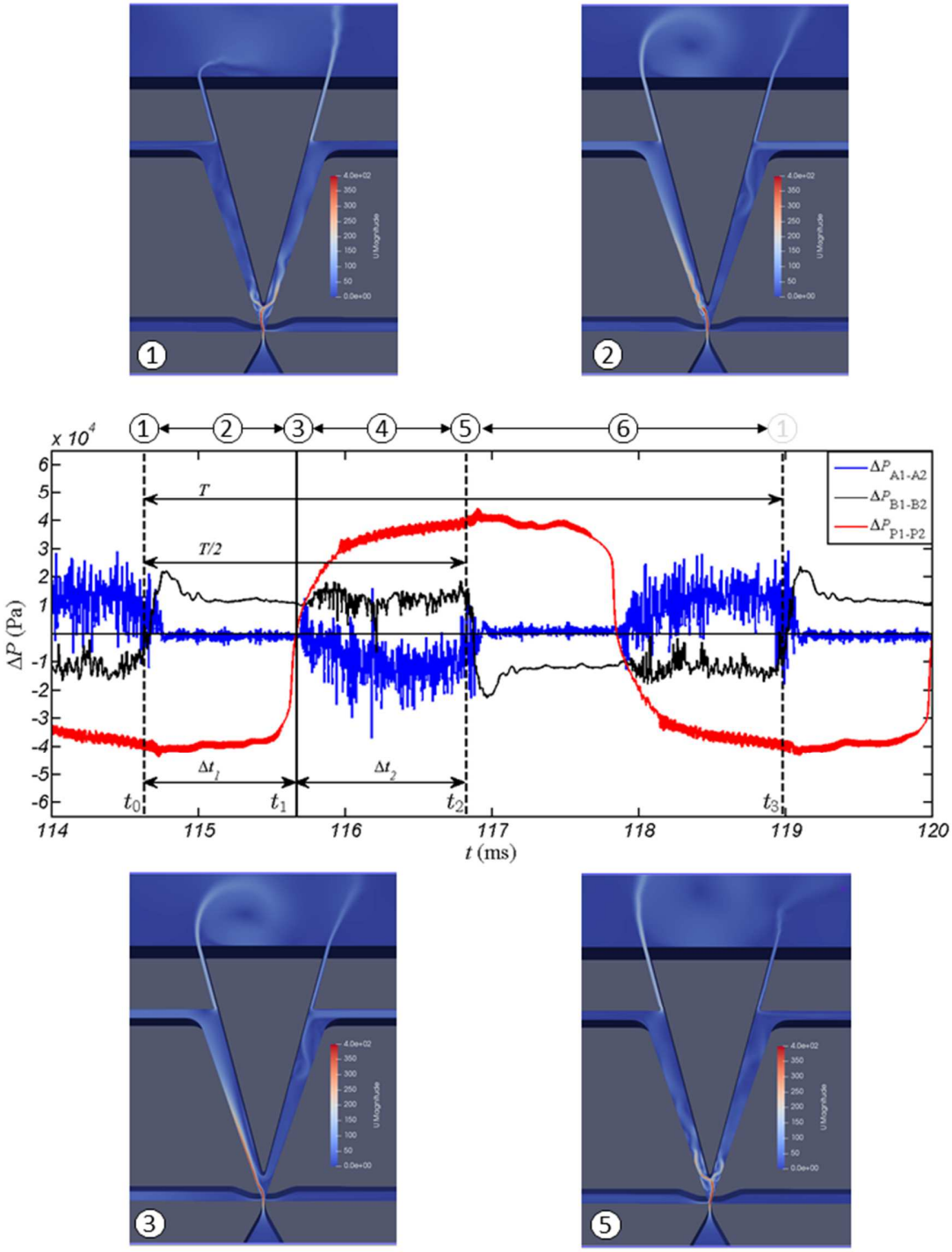

Fig. 6. Evolution of the pressure differences between control ports P, branch inlets A and branch centers B - Numerical simulation for $P_i = 0.25\,MPa$. Snapshots present the velocity contours at four characteristic times of the first half period as described in Section 4.

1- At time t_0, which is defined as the beginning of a period, the main flow jet (MFJ) in the interaction zone is switching from the right side to the left side since the area-averaged velocity U_y at the left outlet is increasing while it is dramatically decreasing at the right outlet, as it can be seen in Fig. 5. At this time, the average value of ΔP_{A1-A2} is about 10 kPa though it is very fluctuating, while the value of ΔP_{B1-B2} increases and becomes positive.

2- Shortly after time t_0, the MFJ is attached to the left branch, thus the left side velocity reaches a maximum value and the right side a minimum, but still positive, value. A high pressure compression wave (HPCW) propagates along the left feedback loop with a velocity $C_o + u_1$, where C_o is the sound velocity (≈340 m/s), and u_1 is the local fluid velocity in front of the wave. This propagation results in a rapid increase of pressure P_{B1} just after time t_0. Simultaneously, in the right side, there is a low pressure expansion wave (LPEW) that propagates along the right feedback loop leading to a rapid decrease of pressure P_{B2}. Accordingly, the value of ΔP_{B1-B2} increases up to its highest value. The value of ΔP_{A1-A2} remains close to 0, which can be explained as sections A1 and A2 are close to each other and the flow in this region is quite steady since ΔP_{P1-P2} is negative and its absolute value is large enough to perfectly attach the MFJ to the left branch although ΔP_{B1-B2} is positive. There is no major change up to time t_1, except a slight decrease of ΔP_{B1-B2} and a slight increase of ΔP_{P1-P2}. The duration $\Delta t_1 (= t_1 - t_0)$ of this step is about 0.23 *T,* where *T* is the simulated oscillation period. *T* = 4.3 *ms* in the present simulation.

3- At time t_1, the HPCW reaches section P1 and the LPEW reaches section P2 almost simultaneously; the value of ΔP_{P1-P2} suddenly reverses from its large negative value just before t_1 to a positive value. From this time, the values of U_y in both exits become more fluctuating since the attachment of the MFJ to the left wall becomes unstable due to the perturbation generated by the positive pressure difference ΔP_{P1-P2}. However, this pressure difference between the two sides of the jet base is not able to provoke the MFJ switching, though it makes it very unstable. The value of ΔP_{A1-A2} becomes negative, which may also prevent the switching.

4- After time t_1, the HPCW and LPEW are reflected back after impacting the base of the jet in sections P, and they continue propagating back along the feedback loops. When they reach sections A1 and A2, at time t_2, the previously negative value of ΔP_{A1-A2} suddenly increases up to about 0 and provokes the MFJ switching from left to right side, as indicated by the inversion of the velocities in both exits. As long as ΔP_{A1-A2} is negative, before time t_2, this pressure difference has a counter effect that prevents the jet switching. Once the pressures between sections A1 and A2 are balanced, the pressure difference ΔP_{P1-P2} at the base of the jet becomes able to provoke the jet switching.

5- Time t_2 corresponds to the end of the first half-period.

6- After this time, the second half-period begins with a symmetric behavior and the whole period is completed at time t_3, as shown in Fig. 5 and Fig. 6. The duration $\Delta t_2 (= t_2 - t_1)$, is about 0.27 *T*.

The main conclusion of the above analysis is that the pressure difference between the control ports at the jet base is not sufficient to cause the jet switching, which only occurs when, in addition, the counter effect of the pressure difference between the two branches is reduced enough, due to the reflected propagation of the pressure waves in the feedback loops.

It can also be observed from Fig. 5 and Fig. 6 that Δt_2 is a bit longer than Δt_1, because the HPCW propagates back along the left feedback loop once it is reflected with a velocity $C_o - u_2$, where u_2 is the local fluid velocity in front of the reflected wave. From t_0 to t_1, the wave propagation direction is the same as the air flow direction while they are in opposite directions from t_1 to t_2, leading to a lower wave propagation velocity in the later period, resulting in $\Delta t_1 < \Delta t_2$. Thus, period *T* can be written as:

$$T = \frac{1}{f} = 2(\tau_t + \tau_s) = 2\left(\frac{L_f}{C_o + u_1} + \frac{L_f}{C_o - u_2} + \tau_s \right) \qquad (2)$$

where τ_t and τ_s are the transmission time and switching time respectively. L_f is the feedback loop length from section A to section P. Introducing the Mach number in front of the wave in the first step of the period $Ma_1 = u_1 / C_0$ and the Mach number in front of the reflected wave in the second step of the period $Ma_2 = u_2 / C_0$, Eq. 2 can be recast as follows:

$$T = \frac{2L_f}{C_o}\left(\frac{1}{1+Ma_1}+\frac{1}{1-Ma_2}\right)+2\tau_s \qquad (3)$$

In general, u_1 and u_2 are small but not negligible compared to the sound velocity ($Ma_2 < Ma_1 \leq 0.2$ according to the numerical simulations), especially when the supply pressure of the oscillator is low. Then, Eq. 3 could be approximated by:

$$T \approx \frac{2L_f}{C_o}\left(1-Ma_1+1+Ma_2\right)+2\tau_s, \qquad (4)$$

which can be expressed as:

$$T \approx \frac{4L_f}{C_o}\left(1+\frac{\Delta Ma}{2}\right)+2\tau_s, \qquad (5)$$

where $\Delta Ma = Ma_2 - Ma_1$ takes into account the asymmetry in wave propagation within the feedback loop, since $\Delta Ma \leq 0$.

It is worth noticing that both Ma_1 and Ma_2 are not accessible in practice. Anyway, assuming that the influence of the wave propagation asymmetry is small in comparison to the leading order term and that τ_s is negligible compared to the whole period T, Eq. 5 reduces to

$$T = \frac{1}{f} = \frac{4L_f}{C_o} \qquad (6)$$

Interestingly, this relationship differs by a factor 2 from that proposed by Simões et al (2005), which is induced by the back and forth wave propagation in the feedback loop.

5 Computational study of the effects of the pressure differences between the two branches and the two control ports

The above-obtained results suggest that the jet switching is not only controlled by the pressure difference at the base of the jet, but also by the pressure difference between the two branches. In order to confirm this assumption, a simplified geometry, which represents the central part of a typical oscillator, has been chosen, as shown in Fig. 3b. This simplified oscillator has the same dimensions as the above simulated oscillator but without feedback loops.

Pressures at both branch outlets (sections G1 and G2) and loop outlets (sections E1 and E2) can be set independently. Four series of unsteady simulations were thus carried out with different pressure differences, as detailed in this section, to study the effect of the pressure difference at control ports only (series 1), the effect of the pressure difference at branches only (series 2) or the combined effect of the two pressure differences (series 3 and 4) on the switching process.

In series 1, the inlet total pressure was set to 0.25 MPa, and a static pressure of 0.1 MPa was imposed in sections Gl, G2, El and E2 (case 0), thus $\Delta P_{\mathrm{E2-E1}} = \Delta P_{G2-G1} = 0$. The numerical settings described in section 3 were used for these simulations.

According to the previous analysis in Section 4, the jet switching in the complete oscillator occurs at t ≈117 ms (cf. Fig. 5), approximately 1ms after the maximum pressure difference between the control ports is reached (at $t \approx 116$ ms, cf. Fig. 6). For that reason, the base case (case 0) of series 1 was initiated from $t = 0$ and simulation results obtained after 1ms were used as initial flow field for the four cases run for an additional duration of 1 ms.

Fig. 7 shows the velocity magnitude iso-contours obtained from the performed unsteady simulations after 1ms for the base case (case 0), and after 2ms for the other cases (i.e. 1 ms of base case simulation + 1 additional ms of simulation with modified pressure at control port E2).

According to Fig. 7, in the base case (case 0) the jet is attached to the right branch, despite the small recirculation zone visible between the jet and the wall.

In this first series, the isolated effect of pressure difference between the control ports, $\Delta P_{\mathrm{E2-E1}} = P_{\mathrm{E2}} - P_{\mathrm{E1}}$, was examined by gradually increasing the pressure in section E2 while keeping the pressures in other sections at their initial value. The initial flow field in each simulation of this series was that obtained in the base case 0 as mentioned previously. A total of five simulations, denoted as cases 1-1, 1-2, 1-3, 1-4 and 1-5, were carried out, corresponding to $\Delta P_{\mathrm{E2-E1}} / P_{\mathrm{i}}$ equal to 0.14, 0.24, 0.28, 0.36 and 0.4, respectively. According to Fig. 7, as $\Delta P_{\mathrm{E2-E1}}$ is increasing gradually, the jet gets more and more bended with even an attachment of the jet base to the left wall. Nevertheless, the jet always flows out through the same outlet (right one), whatever $\Delta P_{\mathrm{E2-E1}}$ is at the control ports, proving that the switching cannot occur if the pressures in the two branches are kept at their initial level. This was also confirmed by additional simulations, starting from the base case which was run for 1ms. $\Delta P_{\mathrm{E2-E1}} / P_{\mathrm{i}}$ was then increased by steps to 0.4, 0.18 and 0.24 for simulations of 1ms on each step. The iso-contours of velocity magnitude at the end of each

of these steps are shown in Fig.SM02 in the Supplementary Material, indicating that the jet switching never occurs, even after 4ms of simulation, at the end of the last step, i.e. a total simulation duration of the order of the complete oscillator period. Video.SM03 in the supplementary material illustrates the non-switching case $\Delta P_{\mathrm{E2-E1}} / P_i = 0.4$ and $\Delta P_{\mathrm{G2-G1}} = 0$.

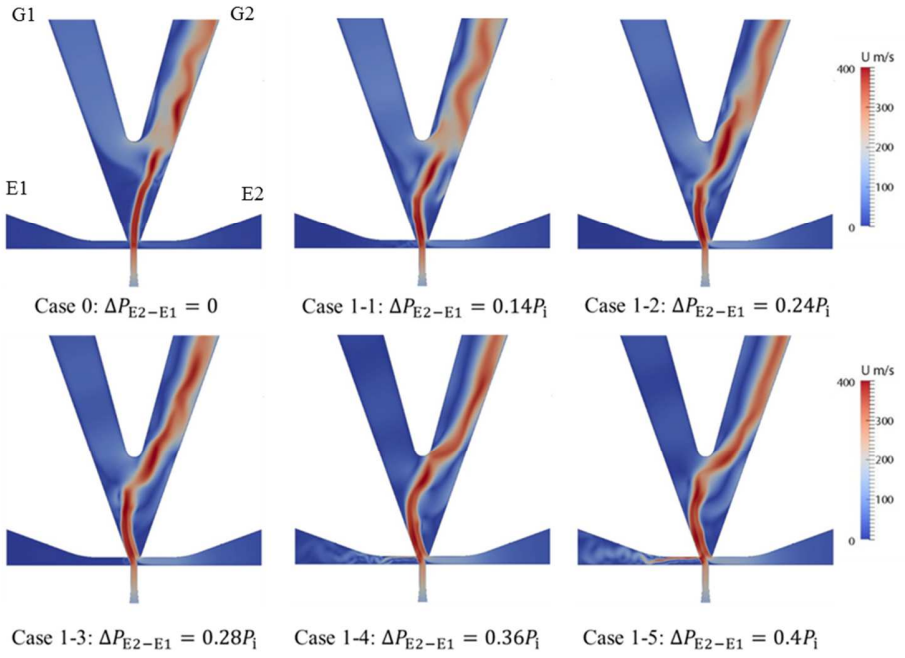

Fig. 7. Iso-contours of velocity magnitude in the simplified oscillator model for different values of $\Delta P_{\mathrm{E2-E1}}$. $P_i = 0.25\,\mathrm{MPa}$

In series 2, the isolated effect of pressure difference $\Delta P_{\mathrm{G2-G1}} = P_{\mathrm{G2}} - P_{\mathrm{G1}}$ between the branches was examined by gradually increasing the pressure in section G2 while keeping the pressures in other sections at their initial value. The initial flow field in this series was the same as in series 1 (case 0). Video.SM04 in the supplementary material illustrates the non-switching case $\Delta P_{\mathrm{E2-E1}} / P_i = 0$ and $\Delta P_{\mathrm{G2-G1}} / P_i = 0.08$.

In series 3, the combined effect of increasing $\Delta P_{\mathrm{G2-G1}}$ with a fixed value of $\Delta P_{\mathrm{E2-E1}} > 0$ was examined. The initial flow field was obtained from series 1 when $\Delta P_{\mathrm{E2-E1}} / P_i = 0.14$, 0.24 and 0.32, for which no jet switching was

observed. Video.SM05 in the supplementary material illustrates the switching case $\Delta P_{E2-E1} / P_i = 0.14$ and $\Delta P_{G2-G1} / P_i = 0.12$

In series 4, the combined effect of increasing ΔP_{E2-E1} with a fixed value of $\Delta P_{G2-G1} > 0$ was examined. The initial flow field was obtained from series 2 when $\Delta P_{G2-G1} / P_i = 0.04$, for which no jet switching was observed.

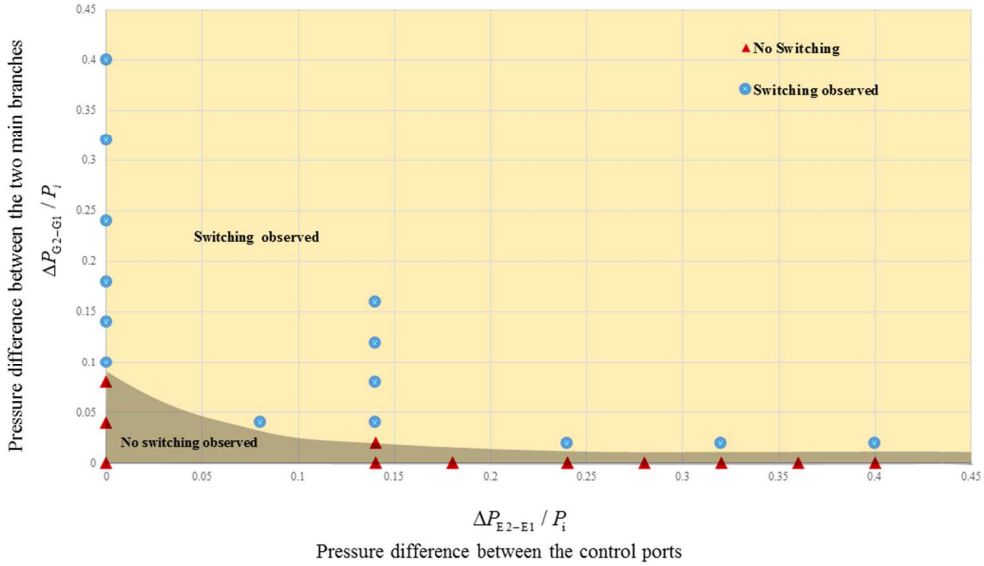

Fig. 8. Jet switchability chart according to ΔP_{E2-E1} and ΔP_{G2-G1} values – Results from numerical simulations

Fig. 8 shows the distribution of all the studied cases according to the pressure differences between the control ports and between the branches. The cases where the jet switches are represented by a circular point, the other ones by a diamond point. From this repartition, it is possible to draw the switchability chart in which two zones can be defined: the small zone in gray at low ΔP_{G2-G1} values corresponds to non-switching jet configurations, the large zone in yellow at higher values of ΔP_{G2-G1} corresponds to switching jet configurations.

In the case of no pressure difference between the branches ($\Delta P_{G2-G1} / P_i = 0$), the switching of the main jet cannot be caused only by a pressure difference ΔP_{E2-E1} between the control ports, whatever its value. On the other hand, the pressure difference between the branches must overcome a certain threshold ($\Delta P_{G2-G1} / P_i = 0.1$) to provoke the

jet switching when the pressure difference between the control ports is zero. This threshold decreases with increasing the pressure difference between the control ports and stabilizes on a small non-zero value for ($\Delta P_{E2-E1} >$ 0.25) and upper. As a conclusion, main jet switching cannot be obtained with only a pressure difference between the control ports but always needs a non-zero pressure difference between the branches. Finally, an interesting observation was made during this computational study: increasing the pressure difference either between the branches or the control ports (ΔP_{G2-G1} or ΔP_{E2-E1}) resulted in significant reductions of the switching time, i.e. the time needed for the jet from the beginning of the simulation to switch to the other branch. This numerical switching time was indeed of the order of 0.4 ms for the lowest values of the pressure difference between the branches leading to the jet switching ($\Delta P_{G2-G1} / P_i = 0.1$) and decreased down to about 0.02 ms for the highest tested values of ΔP_{G2-G1} . Additional numerical simulations are however needed for a better characterization of the jet switching dynamics in relation with the pressure conditions in branches and control ports.

6 Experimental data and analysis

The numerical studies presented in the previous sections revealed the internal dynamics of the oscillator as well as the detailed switching process and key control variables, which are very difficult to analyze experimentally. In order to validate and complete these numerical results, an experimental characterization of the effect of the oscillator's feedback loop length and of the supply pressure on the oscillator dynamic behavior have been performed, thanks to hot-wire anemometry and pressure measurements, as described in Section 3.

6.1 Validation of computational model with Osc.1

The velocity signals at the center of both outlets of Osc.1 (flat design) shown in Fig.9-A were recorded using a hot wire anemometer (wire diameter 3.8µm, wire length 1.27mm) for an inlet pressure $P_i = 0.2\text{MPa}$. Since the hot wire is insensitive to the velocity direction, the small peaks following each large peak are expected to correspond to a negative velocity, directed towards the oscillator, and revealing a suction step after each blowing step. This suction flow is sought in active flow control applications [32]. The maximum velocities in both outlets are similar, with a mean value around 70 m/s. It can be observed, however, that the blowing duration, ΔT_2 , is significantly longer at the left outlet than at the right one, which demonstrates that the internal geometry of the oscillator is not totally symmetrical and that the jet issuing from the nozzle spends more time in the left part than in the right one. These

minor deviations between the prototype's actual internal dimensions and the model that is used for the numerical simulations are due to assembling constraints. In order to validate the numerical results obtained in section 4 for a totally symmetrical geometry, flow simulations based on the actual **non-symmetrical** geometry of the experimental oscillator, obtained by X-ray visualization, were carried out with the same numerical settings used in Section 4.

Comparing the results of both computational studies, it was found that the geometry deviations observed on the real device do not modify the internal flow structure but only the duration of the different phases observed during one oscillation period, with a deviation in frequency of less than 5%.

The evolutions with time of the velocity magnitude in the center of both left and right outlet slots for Osc.1, obtained from the numerical simulations on the scanned non-symmetrical geometry, are presented in Fig.9-B, and are compared to data obtained from hot wire measurements (Fig.9-A). The measured and simulated frequencies are very close with deviation of about 5%. The simulated maximum velocity for Osc.1 is about 110 m/s, which is however higher than the measured 70 m/s. This deviation of about 50% on the maximum velocity could be due to several factors: uncertainties on the measurement of the geometrical dimensions, uncertainties on the velocity measurements (in particular, due to the size of the hot wire which was non negligible compared to the width of the outlet slots) and possible 3D effects not taken into account in the numerical simulations. In both measured and simulated results, the suction velocity can be observed and the suction duration in one period in the left outlet slot is shorter than that in the right one, because of the asymmetry observed in the throat region. The simulated maximum suction velocity is about 25 m/s, which is also of the same order than the measured one.

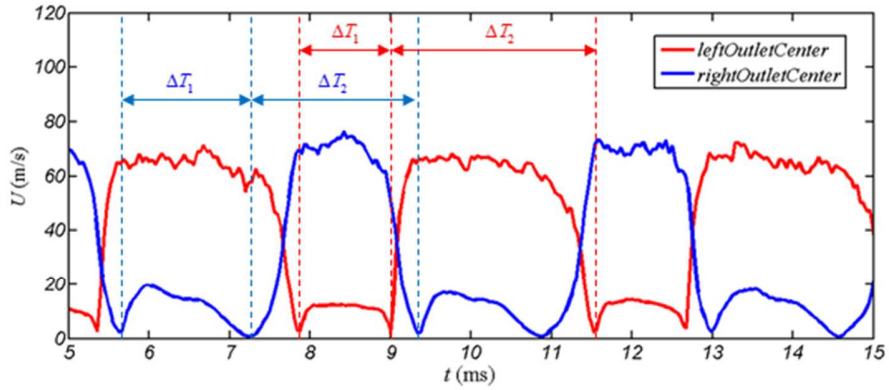

(A) Results from hot wire measurements

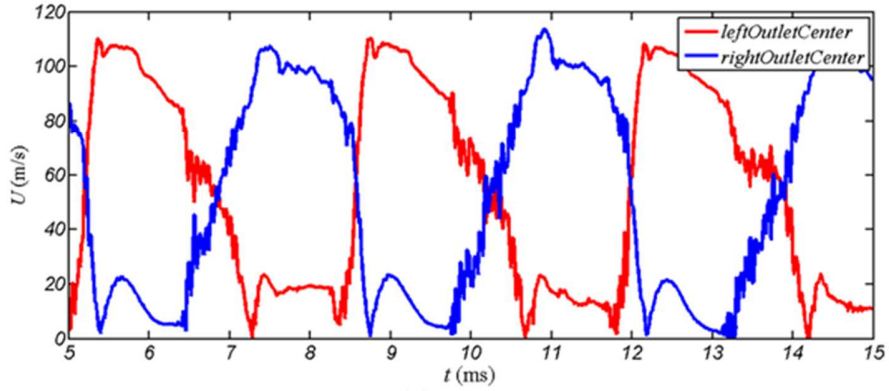

(B) Results from numerical simulation

Fig.9. Experimental and numerical velocity magnitude evolution with time in the center of Osc.1's left and right outlet slots for $P_i = 0.20\,\mathrm{MPa}$

6.2 Frequency response for various feedback loop lengths

The oscillation period is drawn as a function of the inlet pressure in Fig. 10, for both Osc.1 and Osc.2 equipped with feedback loops 4mm in diameter and of different lengths. For inlet pressures $P_i / P_{atm} > 3$, the measured periods are almost constant for each configuration and thus not presented in the figure.

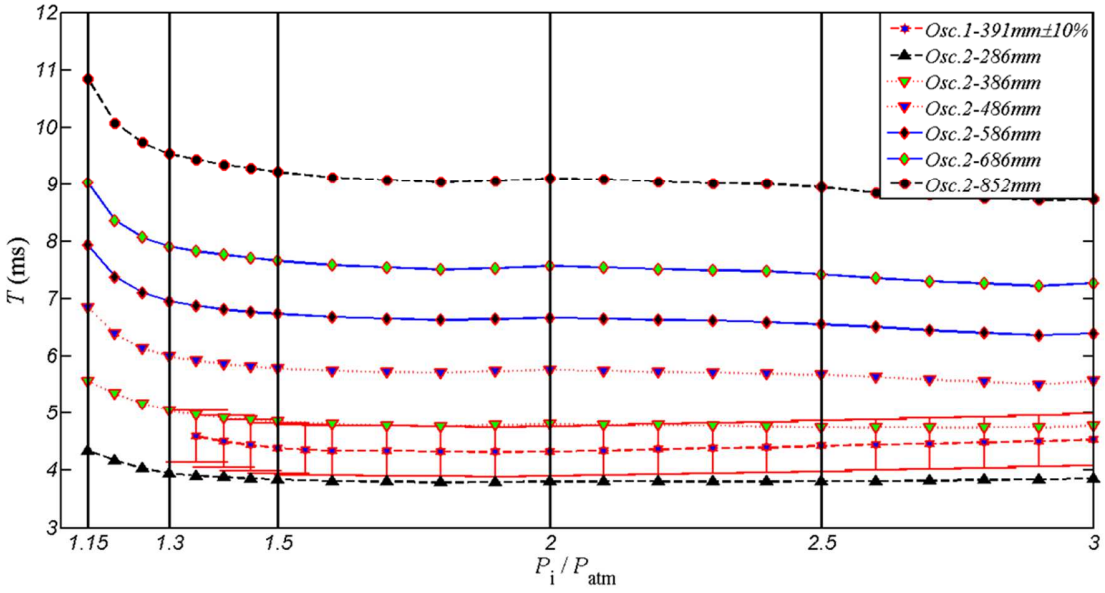

Fig. 10. Oscillation period versus inlet pressure for Osc.1 and Osc.2 with feedback loops 4mm in diameter and for various feedback loop lengths – results from hot wire measurements

In case of Osc.1, the oscillations only begin when the inlet pressure $P_i / P_{atm} > 1.35$, while in case of Osc.2, the oscillations are observed as soon as the inlet pressure $P_i / P_{atm} > 1.15$. This is caused by the real geometry deviations in the switching zone after assemblage, indicating that the oscillation initiation is sensitive to the switching zone shape.

Comparing the measured period of Osc.1, which has a fixed loop length of 391 mm, and that of Osc.2 with a length of 386 mm, 10% deviation is found in resulted oscillation periods with only a 1% variation of L_f. However, it is coherent as the loops of Osc.2 have additional volumes upstream from connecting ports α and downstream from connecting ports β, and in addition 3D effects are present in Osc.2 (see Fig. 4).

The oscillation period decreases with the inlet pressure, down to an almost constant and minimum value reached for inlet pressures $P_i / P_{atm} > 1.7$ for both oscillators and whatever the feedback loop length. This evolution of the oscillation period is similar to the cases of both sonic fluidic oscillators [25] and sweeping fluidic oscillators [33] [34] described in the literature. According to Eq. 5, it can be explained by the fact that $\Delta Ma = Ma_1 - Ma_2$

increases with the inlet pressure when this pressure is low enough to keep the flow subsonic at the nozzle throat, and then becomes almost constant as the flow reaches sonic conditions at the throat, assuming that τ_s remains constant.

For a given P_i, it can be observed that for Osc.2 the period monotonically increases as the feedback loop length increases. This is in accordance with the prediction by Eq. 6 in Section 4, as a result of longer propagation time. With the purpose to further verify the applicability of Eq. 6, the oscillation periods T measured for different feedback loop lengths are drawn in Fig. 11 as a function of the period ($4L_f / C_0$) estimated by Eq. 6 for five values of P_i (0.115, 0.13, 0.15, 0.2 and 0.25 MPa). For each inlet pressure, the oscillation period increases linearly with the length of the feedback loops. However, the slope decreases with increasing P_i. The experimental data fit fairly well the predictions given by Eq. 6 with deviations lower than 15%. It can be clearly observed that when P_i is higher than 0.13 MPa, period T can be approximated by Eq. 6 with a limited error (within 15%), as shown by the dotted lines.

In case of $P_i = 0.115\,\mathrm{MPa}$ (empty circles in Fig. 12), the deviation is more obvious, i.e. more than 15% when $L_f < 0.6\,m$ ($4L_f / C_0 < 7\,ms$), but the slope is closer to the estimated one. Looking at Eq. 3, the larger deviation can be explained by the fact that for this low value of P_i, the pressure differences obtained in branches and control ports are low, leading to larger values of the switching time τ_s, which is neglected in the linear relation Eq. 6. On the other hand, when P_i is very low, much less fluid flows back to the jet base along the feedback loop. In that case, terms $1/(1+Ma_1)$ and $1/(1+Ma_2)$ in Eq. 3 can be approximated to 1, which leads to a slope close to unity in the linear relation between T and $4L_f / C_0$.

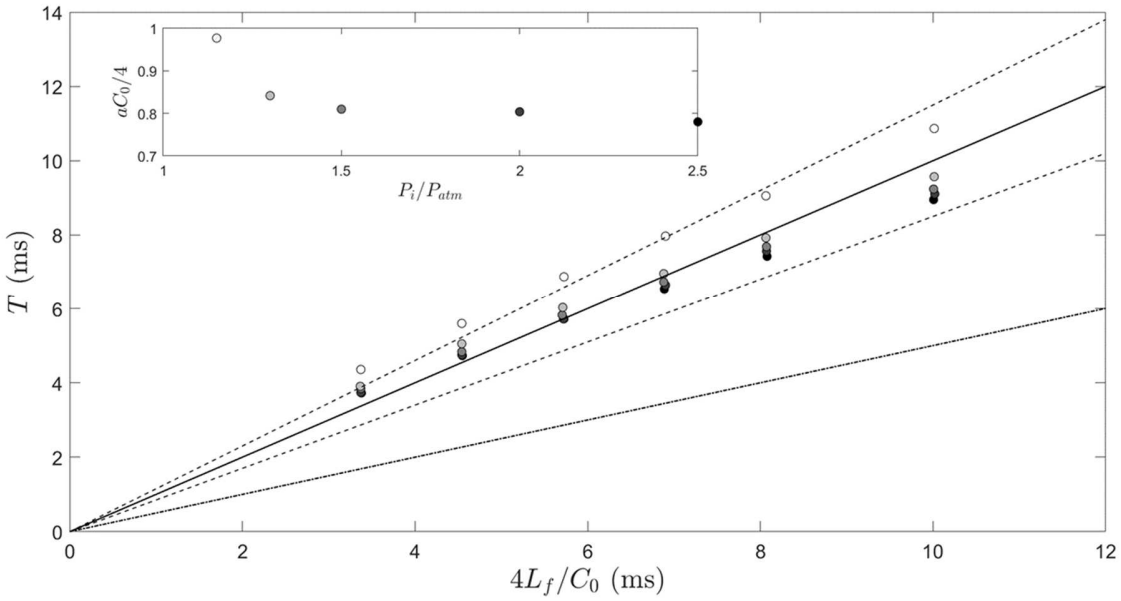

Fig. 11. Oscillation period as a function of the feedback loop length for several inlet pressures. Results from hot wire measurements are represented by circles. The black solid line represents the prediction according to Eq. 6: $f = 4(L_f / C_0)$. The dashed lines symbolize ± 15% deviation apart from this prediction. The dash-dot line illustrates the prediction proposed by Simões et al. [30]**: $f = 2(L_f / C_0)$. The inset shows the evolution of the dimensionless slope estimated from a linear fit of each dataset with respect to the dimensionless inlet pressure**

7 Conclusions

A detailed 2D numerical analysis of the internal flow pattern of a model Coanda fluidic oscillator has been performed in this study, evidencing the role on the oscillation process of the forth and back displacement of compression and expansion waves in the branches and the feedback loops of the oscillator. This has permitted to draw up a new relation for the calculation of the oscillation frequency, which can be simplified assuming that the flow velocity in the loops is low compared to the sound velocity and that the switching time is negligible. In that case, the oscillation frequency is shown to be proportional to the feedback loop length.

Additional numerical simulations focused on the jet switching zone revealed that the jet switching in the Coanda fluidic oscillator studied in the present work is not controlled by the sole pressure difference between the two control ports, but by a combination of this pressure difference and the one between the oscillator's branches.

In order to verify and validate the dynamics revealed by the simulations, two oscillators were designed, manufactured and tested. For the first model close to a 2D configuration (i.e. large depth over width ratio for all the channels), the measured oscillation frequency has been well estimated by the simplified relation deduced from the numerical simulations. The effect of feedback loop length was explored by using the second oscillator prototype with changeable feedback loops made by tubes of same cross-section area than in the 2D model. It was also found that the proposed simplified relation was able to predict the oscillation frequency with a deviation lower than 15%, except in the case of very low inlet pressures. However, the numerical analysis performed in the first part of this work permitted to explain the origin of this limited deviations.

8 References

[1] S. Aubrun, J. Mcnally, F. Alvi, A. Kourta, Separation flow control on a generic ground vehicle using steady microjet arrays, Exp. Fluids. 51 (2011) 1177–1187. doi:10.1007/s00348-011-1132-0.

[2] L.P. Melton, C. Yao, J. Harris, Active Flow Control at Low Reynolds Numbers on a NACA 0015 Airfoil, in: AIAA (Ed.), 26th Appl. Aerodyn. Conf., Honolulu, Hawaii, 2008: pp. 1–18.

[3] C.-Y. Lin, F.-B. Hsiao, Experimental Study of Flow Separation over NACA633018 Wing with Synthetic Jet Control at Low Reynolds Numbers, J. Mech. (2012) 1–8. doi:10.1017/jmech.2012.120.

[4] F. Sun, R.-S. Lin, M. Haas, T. Brogan, Air flow control by fluidic diverter for low nox jet engine combustion, in: AIAA (Ed.), 1st Flow Control Conf., AIAA, St. Louis, Missouri, 2002: pp. 1–8.

[5] D. Guyot, B. Bobusch, C.O. Paschereit, S. Raghu, Active Combustion Control Using a Fluidic Oscillator for Asymmetric Fuel Flow Modulation, in: 44th AIAA/ASME/SAE/ASEE Jt. Propuls. Conf. Exhib., AIAA, Hartford, CT, 2008: pp. 1–19. doi:10.2514/6.2008-4956.

[6] C. Camci, F. Herr, Forced Convection Heat Transfer Enhancement Using a Self-Oscillating Impinging Planar Jet, J. Heat Transfer. 124 (2002) 770. doi:10.1115/1.1471521.

[7] Z. Trávníček, T. Vít, Impingement heat/mass transfer to hybrid synthetic jets and other reversible pulsating jets, Int. J. Heat Mass Transf. 85 (2015) 473–487. doi:10.1016/j.ijheatmasstransfer.2015.01.125.

[8] D. Greenblatt, I.J. Wygnanski, The control of flow separation by periodic excitation, Prog. Aerosp. Sci. 36 (2000) 487–545.

[9] T. Berk, T. Medjnoun, B. Ganapathisubramani, Entrainment effects in periodic forcing of the flow over a backward-facing step, Phys. Rev. Fluids. 2 (2017) 1–18. doi:10.1103/PhysRevFluids.2.074605.

[10] S. Alimohammadi, P. Dinneen, T. Persoons, D.B. Murray, Thermal management using pulsating jet cooling technology, J. Phys. Conf. Ser. 525 (2014). doi:10.1088/1742-6596/525/1/012011.

[11] L.N. Cattafesta III, M. Sheplak, L.N. Cattafesta, M. Sheplak, Actuators for Active Flow Control, Annu. Rev. Fluid Mech. 43 (2011) 247–272. doi:10.1146/annurev-fluid-122109-160634.

[12] C. Cerretelli, E. Gharaibah, An Experimental and Numerical Investigation on Fluidic Oscillators For Flow Control, 37th AIAA Fluid Dyn. Conf. Exhib. (2007) 1–9. doi:10.2514/6.2007-3854.

[13] J.W. Gregory, J.P. Sullivan, G. Raman, S. Raghu, Characterization of the Microfluidic Oscillator, AIAA J. 45 (2007) 568–576. doi:10.2514/1.26127.

[14] B.C. Bobusch, R. Woszidlo, J.M. Bergada, C.N. Nayeri, C.O. Paschereit, Experimental study of the internal flow structures inside a fluidic oscillator, Exp. Fluids. 54 (2013). doi:10.1007/s00348-013-1559-6.

[15] J.W. Gregory, M.N. Tomac, A Review of Fluidic Oscillator Development and Application for Flow Control,

in: AIAA (Ed.), 43rd Fluid Dyn. Conf., San Diego, CA, 2013: pp. 1–26. doi:10.2514/6.2013-2474.
[16] S. Raghu, Fluidic oscillators for flow control, Exp. Fluids. 54 (2013) 1–11. doi:10.1007/s00348-012-1455-5.
[17] G. Raman, S. Raghu, Cavity Resonance Suppression Using Miniature Fluidic Oscillators, AIAA J. 42 (2004) 10–13. doi:10.2514/1.21638.
[18] S. Raghu, Feedback-free fluidic oscillator and method, United States Patent-USOO6253782B1, 2001.
[19] C. Cerretelli, K. Kirtley, Boundary Layer Separation Control With Fluidic Oscillators, J. Turbomach. 131 (2009) 041001. doi:10.1115/1.3066242.
[20] V. Tesař, K. Peszynski, Strangely behaving fluidic oscillator, EPJ Web Conf. 45 (2013) 1–6. doi:10.1051/ epjconf/ 20134501074.
[21] E.W. Simões, R. Furlan, R. Eduardo, B. Leminski, M.R. Gongora-rubio, M. Tadeu, N. Itiro, J.J. Santiago, E.W. Simões, R. Furlan, R.E. Bruzetti Leminski, M.R. Gongora-rubio, M.T. Pereira, N.I. Morimoto, J.J. Santiago Avilés, Microfluidic oscillator for gas flow control and measurement, Flow Meas. Instrum. 16 (2005) 7–12. doi:10.1016/j.flowmeasinst.2004.11.001.
[22] W. Gaylord, V. Carter, FLUERICS. 27. FLUERIC TEMPERATURE-SENSING OSCILLATOR DESIGN, 1969. http://www.dtic.mil/docs/citations/AD0689444.
[23] J.R. Tippetts, H.K. Ng, J.K. Royle, A fluidic flowmeter, Automatica. 9 (1973) 35–45. doi:10.1016/0005-1098(73)90010-1.
[24] H. Viets, Flip-Flop Jet Nozzle, AIAA J. 13 (1975) 1375–1379. doi:10.2514/3.60550.
[25] S. Hayashi, S. Kamaya, A study on mechanism of oscillation in sonic oscillators : 2nd Report, Mathetmatical model of oscillators operated by air, Bull. JSME. 18 (1975) 1035–1043.
[26] G. Raman, E.J. Rice, D.M. Cornelius, Evaluation of Flip-Flop Jet Nozzles for Use as Practical Excitation Devices, J. Fluids Eng. 116 (1994) 508. doi:10.1115/1.2910306.
[27] R. Khelfaoui, S. Colin, S. Orieux, R. Caen, L. Baldas, Numerical and experimental analysis of monostable mini- and micro-oscillators, Heat Transf. Eng. 30 (2009) 121–129. doi:10.1080/01457630802293548.
[28] G. Arwatz, I. Fono, A. Seifert, Suction and oscillatory blowing actuator, Solid Mech. Its Appl. 7 (2008) 33–44. doi:10.1007/978-1-4020-6858-4_4.
[29] V. Tesař, K. Peszynski, Strangely behaving fluidic oscillator, EPJWeb Conf. 45 (2013) 1–6. doi:10.1051/ epjconf 201/ 34501074.
[30] E.W. Simões, R. Furlan, R.E. Bruzetti Leminski, M.R. Gongora-Rubio, M.T. Pereira, N.I. Morimoto, J.J. Santiago Avilés, Microfluidic oscillator for gas flow control and measurement, Flow Meas. Instrum. 16 (2005) 7–12. doi:10.1016/j.flowmeasinst.2004.11.001.
[31] S. Wang, L. Baldas, S. Colin, S. Orieux, A. Kourta, N. Mazellier, I. Introduction, Experimental and numerical study of the frequency response of a fluidic oscillator for active flow control, in: 8th AIAA Flow Control Conf. AIAA, AIAA Aviation, Washington, D.C., 2016: pp. 1–15. doi:10.2514/6.2016-4234.
[32] A. Seifert, L.G. Pack, Active Flow Separation Control on Wall-Mounted Hump at High Reynolds Numbers, AIAA J. 40 (2002) 1363–1372. doi:10.2514/2.1796.
[33] F. Gosen, F. Ostermann, R. Woszidlo, C. Nayeri, C. Paschereit, Experimental Investigation of Compressibility Effects in a Fluidic Oscillator, Aiaa 2015-0782. (2015) 1–11. doi:10.2514/6.2015-0782.
[34] L.P. Melton, M. Koklu, L.G. Pack Melton, M. Koklu, Active Flow Control using Sweeping Jet Actuators on a Semi-span Wing Model, in: 54th AIAA Aerosp. Sci. Meet., AIAA, San Diego, California, USA, 2016: pp. 1–16. doi:10.2514/6.2016-1817.

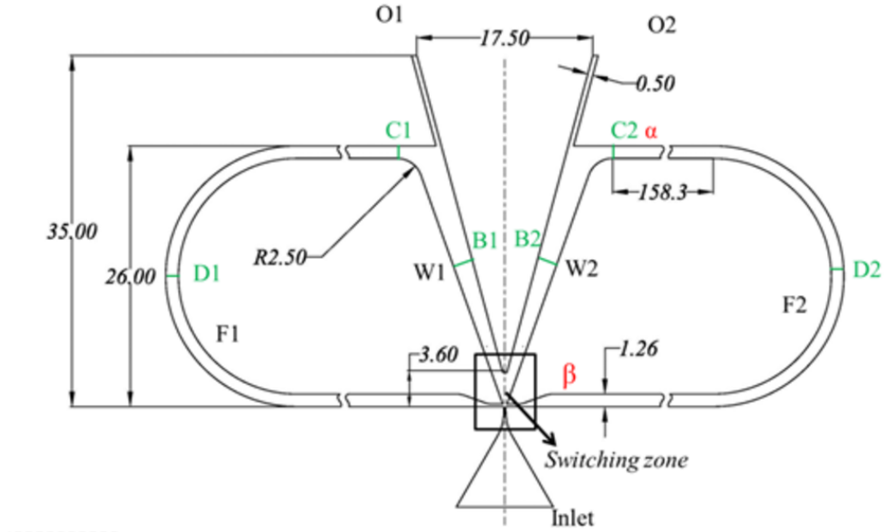

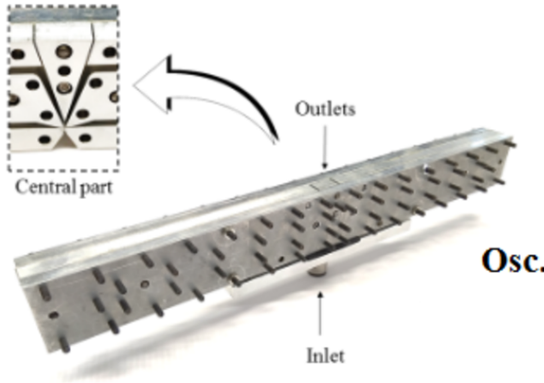

Osc.1 **Osc.2**

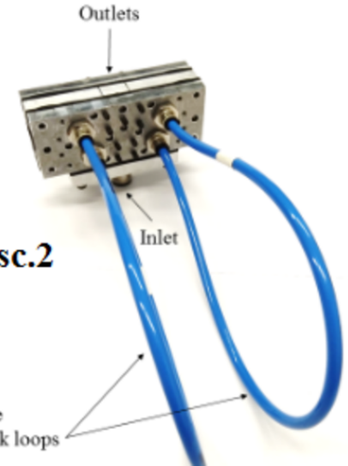

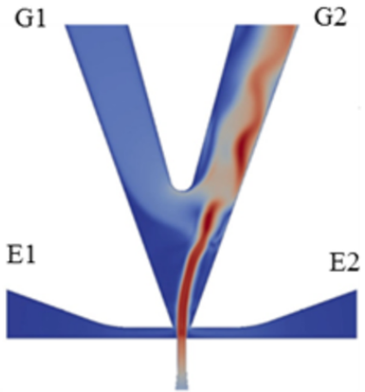

Case 0: $\Delta P_{E2-E1} = 0$

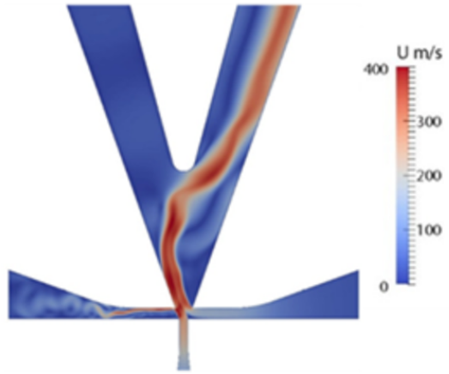

Case 1-5: $\Delta P_{E2-E1} = 0.4P_i$

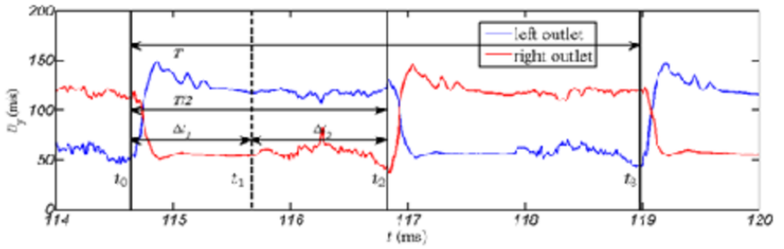

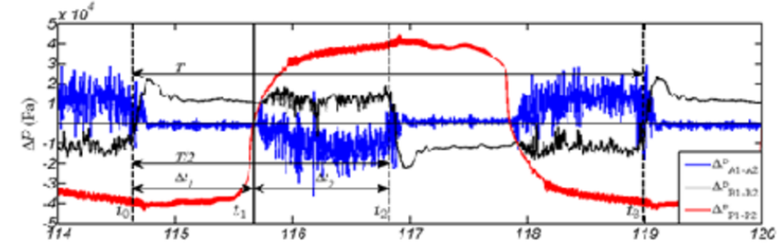

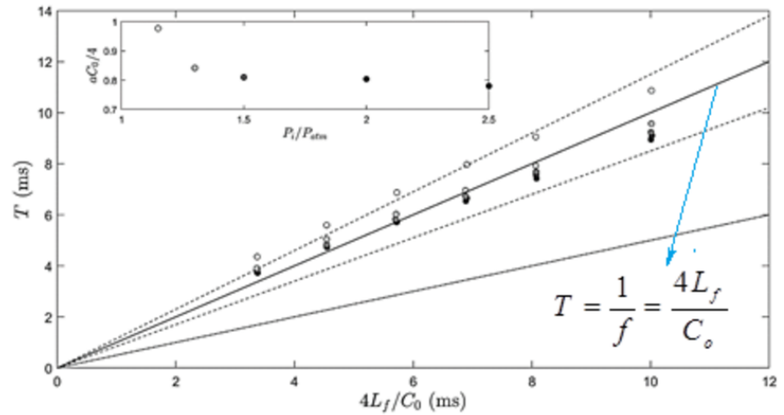

$$T = \frac{1}{f} = \frac{4L_f}{C_o}$$